

Achieving ultra-high strength of Al-Cu-Li alloys by the combination of High Pressure Torsion and age-hardening

Jiahui Dong^a, Nong Gao^{a,*}, Ying Chen^b, Lingfei Cao^c, Hui Song^c, Hannes Fröck^d, Benjamin Milkereit^e, Marco J Starink^a

^a Materials Research Group, Faculty of Engineering and Physical Sciences, University of Southampton, Southampton SO17 1BJ, UK

^b Metal Materials, School of Materials Science and Engineering, Xiamen University of Technology, Xiamen 361024, China

^c International Joint Laboratory for Light Alloys (Ministry of Education), College of Materials Science and Engineering, Chongqing University, Chongqing 400044, China

^d Chair of Materials Science, Faculty of Mechanical Engineering and Marine Technology, University of Rostock, 18059 Rostock, Germany

^e Competence Centre °CALOR, Department Life, Light and Matter, University of Rostock, 18059 Rostock, Germany

* Corresponding author.

E-mail address: n.gao@soton.ac.uk (N. Gao). Tel: +44 (0)23 8059 3396

Abstract

The combined strengthening effects of high pressure torsion (HPT) and age hardening on a recently developed 3rd generation Al-Cu-Li alloy was investigated. Solution treated samples were processed through HPT at room temperature, followed by low temperature artificial ageing (i.e. T4-HPT-AA). A micro-hardness of ~ 240 Hv was achieved on ageing at 110 °C/60h after HPT. A further improvement in the hardness to ~ 260 Hv was accomplished by a pre-ageing 110 °C/24h before HPT combined with a post-HPT ageing process at 110 °C for 180h (i.e. T6-HPT-AA). These novel multi-stage processes give rise to an increase in hardness by a factor of 2 as compared to the T4 condition (~ 120 Hv). After HPT the grain size was dramatically refined to the ultrafine-grained (UFG) structure, accompanied by a large amount of dislocations. No long-range ordered precipitates were observed after HPT and subsequent ageing treatments. Instead, atom probe tomography (APT) provided clear evidence that Cu-Mg co-clusters were homogeneously distributed in the matrix of T4 and T6 processed samples and they segregate strongly to the grain boundaries (GBs) during HPT. Further ageing treatment after HPT leads to the segregation of clusters to dislocations. A strengthening model that incorporates dislocation hardening, grain boundary hardening, solid solution strengthening and a new short-range order strengthening mechanisms was used to predict the yield strength of the alloy. This model indicates that the combined effect due to all three types of Cu-Mg clusters (clustering in matrix, clustering at GBs and at dislocations) is dominant for the strength in all conditions.

1. Introduction

In recent years, under the increasing demand for fuel efficiency and cost efficiency, Al-Cu-Li alloys have gained great attention for their uses in the aircraft industry and aerospace programmes owing to their lightweight combined with a balance of damage tolerance and good formability [1,2]. In particular, they have recently been employed in many advanced aerospace applications such as Boeing 777, Airbus 380, NASA space shuttle in view of their low density, high specific strength and stiffness [3,4]. Such commercially available heat treatable Al alloys are strengthened by age hardening through the formation of nanoscale particles in the grains, that inhibit the dislocation motion [5,6]. Besides, grain refinement can also lead to a significant increase in the strength of metallic materials. Given this, the fabrication of ultra-fine grain (UFG) structure through severe plastic deformation (SPD) is an effective method. As one of the most popular SPD techniques, high pressure torsion (HPT) can produce exceptional levels of grain refinement and achieve a UFG microstructure with a high dislocation density [7].

In the past three decades, the formation of clusters and co-clusters were observed in many Al-based metallic alloys during solution treatment or low temperature ageing [8–11]. These clusters have been accepted to be the dominant strengthening factor due to a short-range order strengthening mechanism [8,9]. More recently, the UFG Al-Cu-Mg (AA2024) [12] and Mg-Gd-Y-Zn [13] alloys processed by HPT showed that the segregation and clustering of solutes at GBs. Such clusters serve as obstacles to grain growth and stabilise the nanosized grains via pinning the grain boundaries, providing an extra strengthening effect in UFG alloys [12,14,15].

To exploit the strengthening mechanisms that contribute to the high strength of HPT-processed metallic alloys, several detailed models which incorporate the grain

refinement and dislocation strengthening contributions were proposed [16–19]. In subsequent works, the solute atoms were also considered as part of strengthening effects, and segregation of solute atoms at grain boundaries was detected in the 7075 and 7136 Al alloys [14,20,21] after SPD processing. On this basis, a physically-based model incorporating solute clusters and segregation cluster-defect complexes strengthening was then established by Chen et al. [22], which successfully predicted the strength of the UFG Al-Cu-Mg alloy. However, this model of cluster strengthening in the absence of detailed explanations for each individual type of cluster strengthening mechanism, i.e. clusters in matrix, clustering at GBs and dislocations. Also, there is a number of research works on the dislocation-solute interaction [11], but little is known about the enthalpy change of clustering at dislocations and amount of strengthening provided by these dislocation-solute complex structures. Hence, in this work, the understanding of the strengthening due to clusters on defects is discussed, and different enthalpy values of different types of clusters are estimated.

Previous studies indicated that the hardness and strength of Al-based alloys can be substantially improved by HPT processing [7,23–25]. Also, many combinations of equal-channel angular pressing (ECAP) and ageing have been successfully used to enhance the strength of Al alloys and especially pre-ECAP solution treatment combined with post-ECAP low temperature ageing has been applied [26–30]. No works have been done to investigate the combination of HPT and age hardening on the Al-Cu-Li alloys.

Therefore, the present work aims to obtain ultra-high strength Al-Cu-Li material via the combined effects of HPT and artificial ageing (AA). To reveal the microstructural evolution, X-ray diffraction (XRD), transmission electron microscopy (TEM) and Differential scanning calorimetry (DSC) are employed. Also, to analyse the behaviour of solute clusters in different processing conditions, atom probe tomography (APT) is

used. Finally, a model is applied to evaluate the contributions of strengthening mechanisms in the strength of the material and predict the strengthening in an Al-Cu-Li alloy during T4-HPT-AA and T6-HPT-AA treatments.

2. Experimental materials and procedures

An experimental Al-2.88Cu-1.34Li-1.03Mg-0.09Zr (wt%) alloy with a composition similar to typical 3rd generation Al-Li alloys was designed with the aim of retaining or optimising the critical mechanical properties of the 2024-T351 alloy, which possesses a yield strength of ~325-350 MPa [31]. The alloy was produced by casting and subsequent rolling at QinetiQ (Farnborough, UK). The samples were cut into disks of 9.8 mm in diameter and mechanically ground to 0.80 ± 0.3 mm in thickness. 5 turns of HPT processing was conducted on these disks at room temperature, using a pressure of 6 GPa and a rotation speed of 1rpm. Two different processing conditions were performed on the samples: (1) Solution treatment + HPT + artificial ageing (i.e. T4-HPT-AA); (2) Solution treatment + artificial ageing + HPT + artificial ageing (i.e. T6-HPT-AA). The full details of processing procedures, including ageing temperature and time are given in Table 1.

Micro-hardness, XRD, TEM, DSC and APT tests were performed on the Al-Cu-Li alloys in all stages of two processing procedures (T4-HPT-AA and T6-HPT-AA) from solution treatment to final ageing hardening aimed at revealing the evolution of the microstructure.

Table 1. The processing details for two processing conditions.

Processing conditions	Processing details
T4-HPT-AA	SSS (515 °C/0.5h) + natural ageing (12h) + HPT + artificial ageing (110 °C/60h)
T6-HPT-AA	SSS (515 °C/0.5h) + pre-ageing (110°C/24h) + HPT + post-ageing (110°C/180h)

Vickers hardness was carried out on mirror-like polished surfaces by a micro-hardness tester employing a dwell time 15s and a load of 300 gf. For each processed sample, five measurements were taken at points half-way between centre and edge of the disks to provide a realistic average hardness. Five measured positions were separated by about 0.5 mm to avoid mutual interference between the different selected points, and the reported hardness for each processed sample is the mean of its five indentations.

XRD was carried out using a Rigaku SmartLab X-ray diffractometer equipped with a graphite monochromator Cu K α radiation at 50 steps per degree and a count time of 1.2s per step. The slit length was chosen as 5 mm. In order to improve accuracy and reduce errors, the data for each sample were collected by repeating runs. The samples with a diameter of 4 mm were punched from HPT-processed discs at the peripheral region (1 mm from the centre). Furthermore, to determine crystallite size and microstrains, XRD line broadening analysis was performed using the Materials Analysis Using Diffraction (MAUD) software that is based on the full peak X-ray profile refinement using the Rietveld method [32,33]. Dislocation density ρ , defined as the length of dislocation lines per unit volume (m/m^3) can be obtained from the measured microstrains and crystallite size from [34]:

$$\rho = \frac{2\sqrt{3}\langle\varepsilon^2\rangle^{1/2}}{D_c b} \quad (1)$$

Where b is the Burgers vector, equal to 0.286 nm for FCC Al materials, D_c is the crystallite size and ε is microstrain.

TEM was conducted on the Al-Cu-Li alloy using a FEI Talos TMF200S TEM/STEM operated at 200 kV. The disk samples were mechanically ground down to $\sim 150 \mu\text{m}$ in thickness first, and smaller disk-shaped samples with 3 mm in diameter were punched at a position 1 mm from the centre of the disk. The samples were then ion-polished

using Gatan PIPS II polishing system through Ar ion beam milling process to obtain a thin electron transparent TEM sample.

DSC measurements were performed on disc-shaped samples with 6.1 mm in diameter and 0.6 mm in thickness punched from the periphery of the processed disc samples using a Perkin-Elmer Pyris Diamond calorimeter. Pure Al samples of similar mass were used as reference samples. Heating was conducted from -50 °C to 320 °C at a constant rate of 30K/min. A Huber TC 100 cooler was used, and the nitrogen gas was purged to provide a protective gas atmosphere.

Needle-shaped specimens for APT analysis were prepared from a thin metal bar with dimensions of 0.5 mm × 0.5 mm × 10 mm using standard two-step electro-polishing procedures. APT analysis was conducted using a LEAP 4000 HR at a specimen temperature of 50 K, a pulse repetition rate of 200 kHz, a pulse voltage fraction of 15% and a target evaporation rate of 0.5%. The background vacuum level of the analysis chamber was less than 10^{-8} Pa, and the detection efficiency was 36%. The reconstruction and visualisation of the APT data were performed using Imago Visualization and Analysis Software (IVAS) 3.6.12 software [35]. Solute-rich features were identified using the maximum separation method, with Cu and Mg as targeting clustering solutes [10]. Mg and Cu atoms were identified as clustered/segregated if they had a separation distance of $d_{max} < 0.7$ nm.

3. Results and analysis

3.1 Micro-hardness measurements

The micro-hardness of Al-Cu-Li alloy samples in T4, T4-HPT, T4-HPT-AA, T6, T6-HPT and T6-HPT-AA conditions were measured. [Fig. 1\(a\)](#) shows that the micro-hardness after T4 treatment (i.e. solution treatment for 515 °C /0.5h followed by quenching and natural ageing for 12h) was ~120 Hv. After 5 turns HPT processing, the

hardness has dramatically increased to ~ 220 Hv, and a continued low temperature ageing treatment ($110\text{ }^{\circ}\text{C}/60\text{h}$) improved the peak-aged hardness further to ~ 235 Hv. On the other hand, processing by T6 treatment (i.e. solution treatment followed by quenching and artificial ageing $110\text{ }^{\circ}\text{C}/24\text{h}$) does not show any improvement in hardness in [Fig. 1\(b\)](#), compared with the sample that had been processed by T4 treatment. Also, it is obvious that the hardness increases strongly from ~ 120 Hv to ~ 210 Hv after processing by HPT. As expected, a further improvement in the hardness to ~ 260 Hv was accomplished by a pre-ageing ($110\text{ }^{\circ}\text{C}/24\text{h}$) before HPT in combination with a post-ageing ($110\text{ }^{\circ}\text{C}/180\text{h}$) process. This gives over twice that of the initial T4-processed sample (~ 120 Hv).

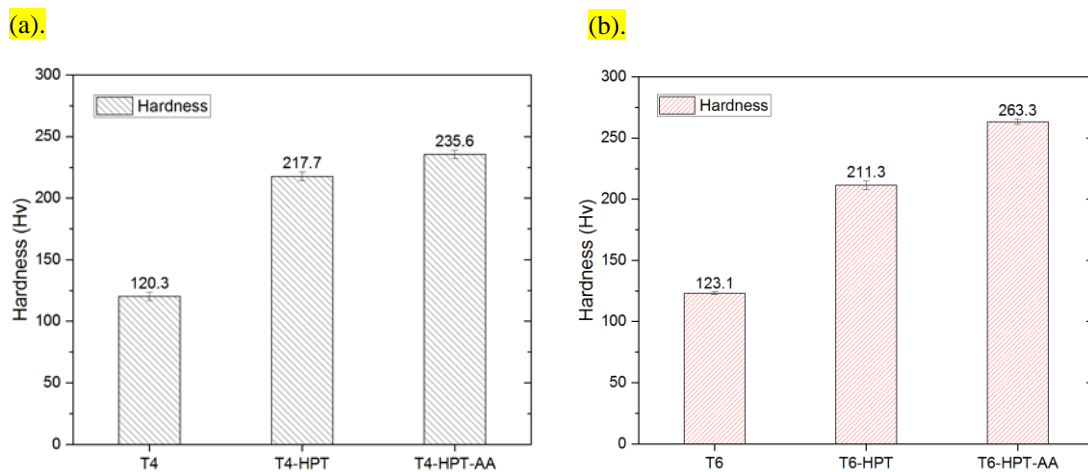


Fig. 1. (a) Vickers hardness of Al-Cu-Li alloy under T4, T4-HPT and T4-HPT-AA; (b) T6, T6-HPT and T6-HPT-AA processing conditions.

3.2. Microstructural characterisation

3.2.1. XRD analysis

XRD diffraction spectra in the range of 30° - 90° were collected for the samples in different processing conditions. In [Fig. 2\(a\)](#), diffraction peaks due to the Al-phase are detected, the observed peaks are due to (1 1 1), (2 0 0), (2 2 0), (3 1 1) and (2 2 2) at 2θ equal to 38° , 45° , 65° , 78° and 82° , respectively. The spectra of the undeformed samples

(i.e. T4 and T6) in addition reveal the presence of additional weak peaks, identified as S (Al_2CuMg) and θ (Al_2Cu) phases. Accordingly, the absence of S and θ phases in the other four conditions suggesting that all these precipitates are dissolved in Al matrix and a supersaturated solid solution forms after HPT processing. Additionally, Al-phase diffraction peaks remain present and no additional peaks arise after HPT or post-ageing treatments indicate no new phases are formed due to post-ageing. Besides, the intensities of Al phase peaks varies with different processing conditions, which indicates that HPT processing changed the crystallographic texture of the alloys. [Fig. 2\(b\)](#) reveals that HPT processing caused peak broadening, which is ascribed to the reduction in crystallite size and increased density of lattice defects [36,37].

The crystallite size and microstrain were optimised simultaneously using Rietveld refinement through profile fitting on the XRD data. [Fig. 3\(a\)](#) shows that the crystallite size of T4-processed sample is reduced by a factor of 10 during 5 turns HPT processing at room temperature, and then slightly increases during the subsequent ageing for 60h. The dislocation densities have an opposite trend: increasing to the highest level of $\sim 3.5 \times 10^{14} \text{ m}^{-2}$ right after HPT, indicates dislocation accumulation during HPT deformation and gives rise to a high hardness. Subsequent peak ageing treatment results in a dropping to $\sim 0.8 \times 10^{14} \text{ m}^{-2}$. It is apparent that the changes in crystallite size and dislocation densities with the consecutive processing conditions T6, T6-HPT and T6-HPT-AA present almost the same trend as with T4, T4-HPT and T4-HPT-AA processing conditions, shown in [Fig. 3\(b\)](#).

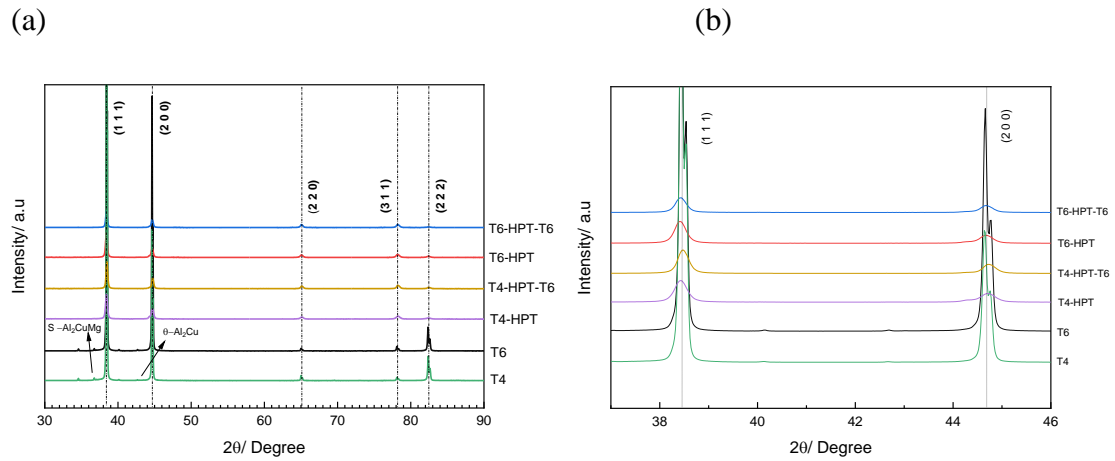


Fig. 2. (a) Overview of XRD patterns of the HPT-processed and aged Al-Cu-Li alloys, (b) enlarged Section of XRD pattern from 37 °C to 46 °C.

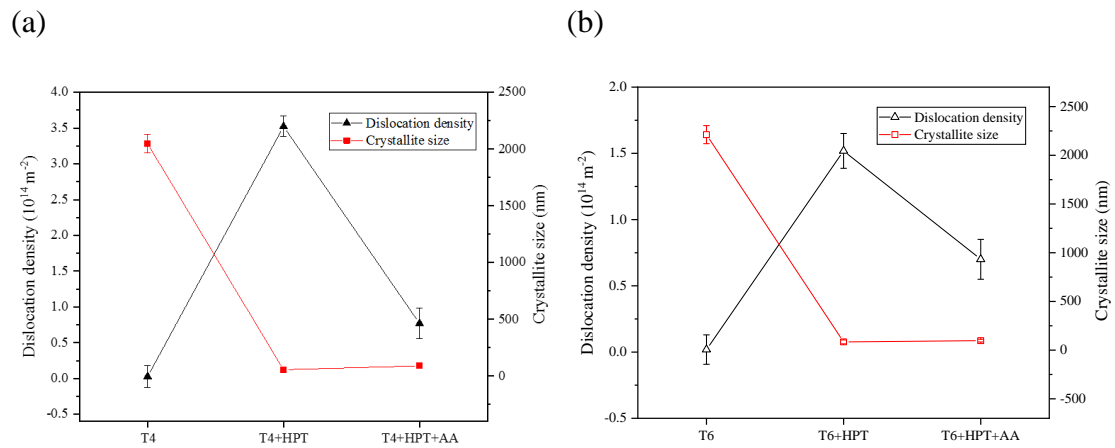


Fig. 3. The crystallite size and dislocation density as a function of different processing conditions; (a) T4, T4-HPT and T4-HPT-AA, and (b) T6, T6-HPT and T6-HPT-AA processing conditions.

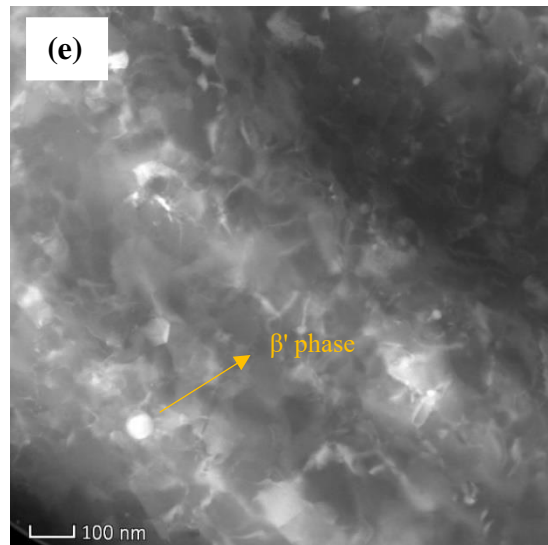
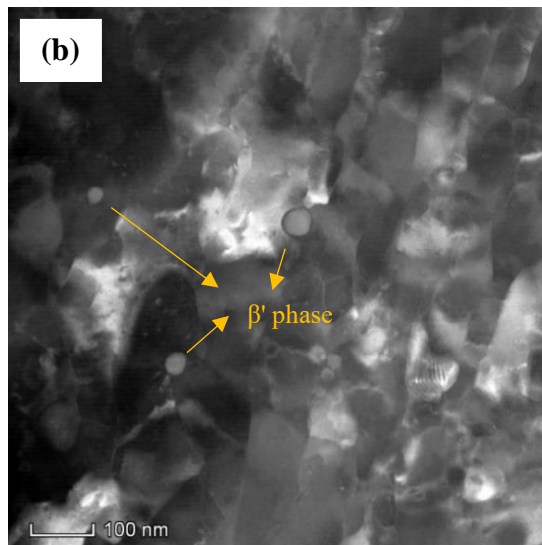
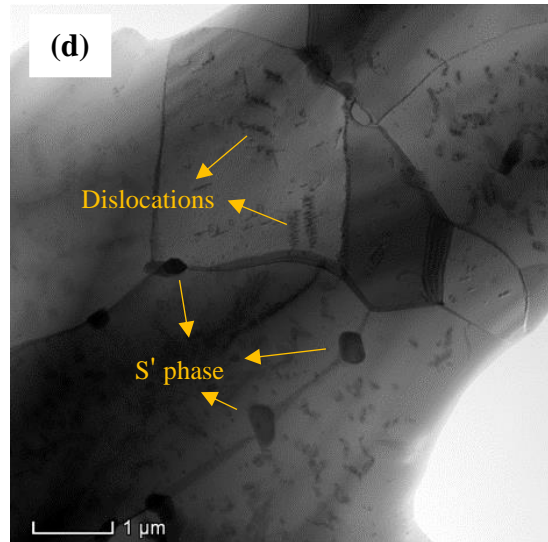
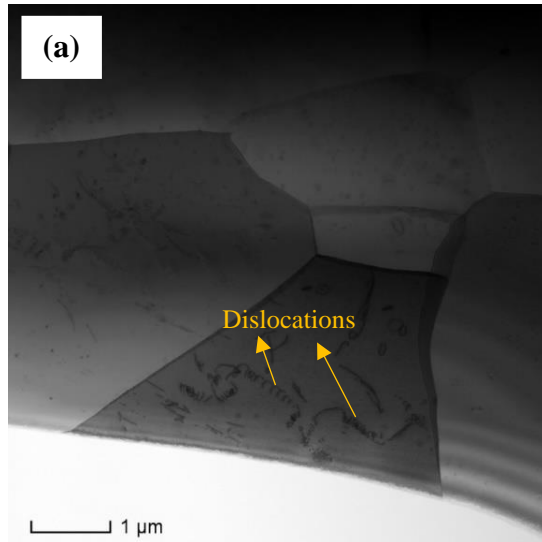
3.2.2 TEM

TEM dark-field micrographs of samples in the different processing conditions are shown in Fig. 4(a)-(f), and the corresponding mean grain sizes were estimated by the line intercept method described in [38]. The undeformed Al-Cu-Li alloys in T4 and T6 conditions have a grain size of 3.0 μm and 3.1 μm . Fig. 4(d) reveals the presence of particles with a size of about 250 nm, mainly located at grain boundaries. The

corresponding elemental mapping was conducted by energy dispersive spectrometry (EDS) detector. It provided further evidence that these particles contain a high concentration of Cu and Mg atoms, and thus they were identified as S' phase (Al_2CuMg), the only known precipitate phase that contains Cu and Mg. After 5-turn HPT, grains with a size of 96 ± 6 nm and 115 ± 13 nm appear in the microstructure of T4-HPT and T6-HPT samples, i.e. the grain size has been reduced significantly by HPT processing, which gives a UFG structure. [Fig. 4\(e and f\)](#) show slight grain growth, compared with as-HPT condition, indicating grain coarsening during subsequent ageing treatment. Eventually, further ageing causes a mean grain size of 102 ± 9 nm and 123 ± 10 nm in the T4-HPT-AA and the T6-HPT-AA conditions.

The spherical-shaped particles with a size of ~ 50 nm were observed throughout all the samples, i.e. it was present right from the start of the processing and is retained even during solution treatment, ageing treatment, and HPT processing, as shown in [Fig. 4\(a\)-\(f\)](#). These particles were detected to be Zr-rich particles by EDS analysis. Comparison with literature data on shape and composition of Zr-rich particles in Al alloys [39–41] indicates that these particles are β' (Al_3Zr) phase. The β' phase particles are observed in many Zr-containing Al alloys after quenching or ageing treatment (see, e.g. [39,41,42]). These particles stabilise the grain growth, inhibit recrystallisation, and effectively pin the grain and sub-grain boundaries, thereby helping to improve the hardness and toughness through influencing grain size and reducing recrystallisation [39]. However, as a very limited amount of β' phase particles form, they will not contribute much to the strengthening of the Al-Cu-Li alloy by themselves. Besides these β' phase particles, TEM does not show any visible precipitates after HPT processing and subsequent ageing treatments. However, similar processing conditions performed on AA2091 (Al-2.09Li-1.99Cu-1.55Mg-0.12Zr in wt%) show that fine δ' (Al_3Li) precipitates exist within the UFGs

after ageing and are responsible for the age hardening [43]. Apparently, the lower content of Li in our alloy (1.34 wt% Li) compared with AA2091 (2.09 wt% Li) makes it unlikely to form δ' phase. Also, the temperature here (~ 110 °C) is too low to cause nucleation of precipitates.



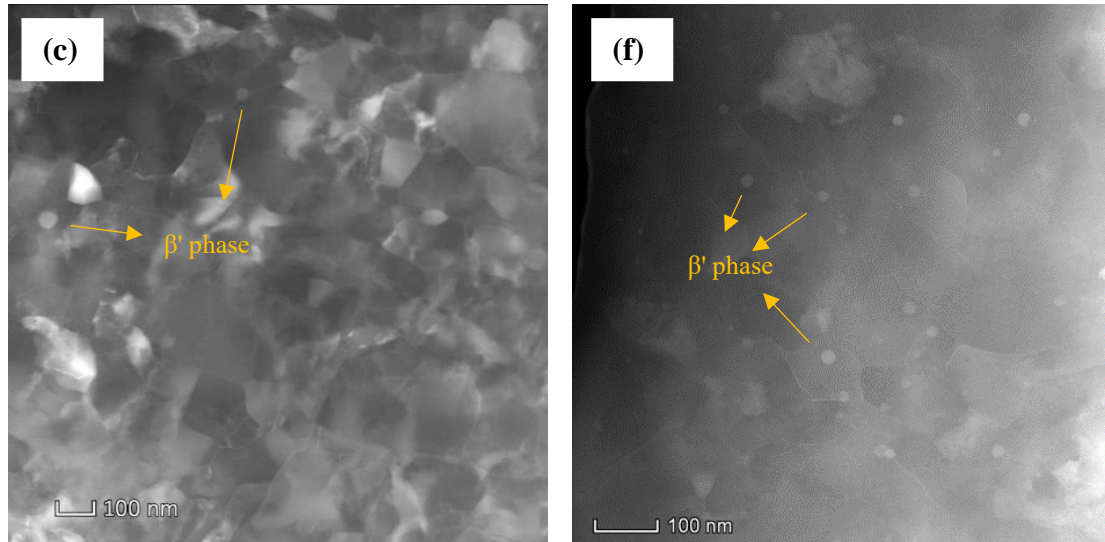


Fig. 4. TEM dark-field images showing the structural evolution of Al-Cu-Li alloy in (a) T4, (b) T4-HPT, (c) T4-HPT-AA, (d) T6, (e) T6-HPT (f) T6-HPT-AA conditions.

3.3 Solute segregation and clustering

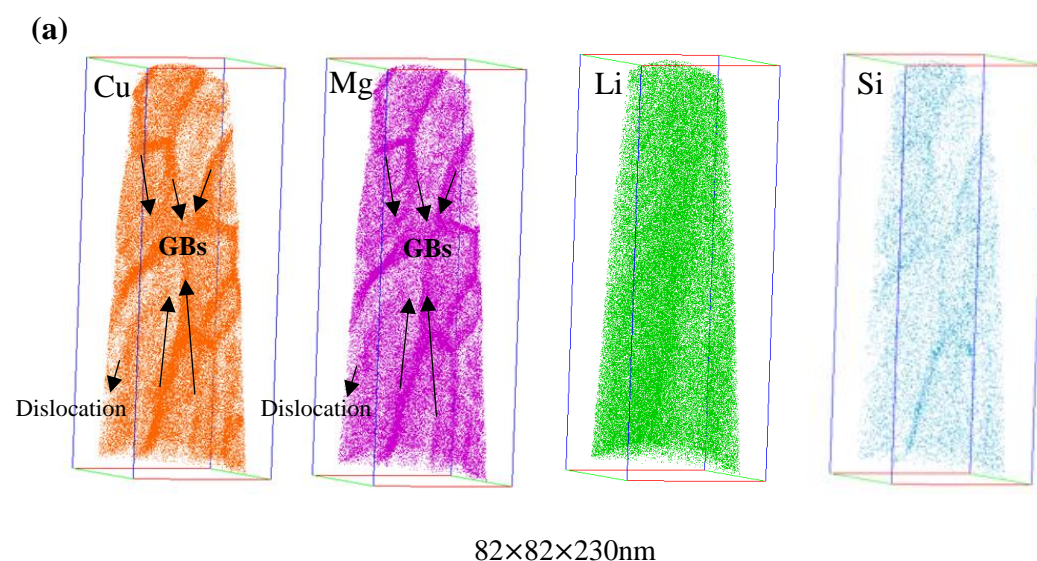
[Fig. 5](#) and [Fig. 6](#) show the APT atom maps of alloying elements Cu, Mg, Li and impurity element Si for the samples processed by T4-HPT-AA and T6-HPT-AA treatments, respectively. The analysed volume of both samples comprises three forms of solute enriched feature, i.e. at segments of the grain boundaries, at a dislocation line, and in the grain away from these defects.

Six GBs have been analysed in T4-HPT-AA condition and five GBs have been analysed in T6-HPT-AA condition, marked with black arrows in [Fig. 5\(a\)](#) and [Fig. 6\(a\)](#). The typical concentration profile of solutes across the GBs in T4-HPT-AA and T6-HPT-AA conditions are shown in [Fig. 5\(b\)](#) and [Fig. 6\(b\)](#), which reveals the segregation of Cu and Mg solutes at the GB in both conditions. The atomic concentration ratio of segregation of Cu: Mg at the grain boundaries is approximately 1:1. Additionally, segregation of Cu and Mg solutes at a dislocation was evident in [Fig. 5\(c\)](#) and [Fig. 6\(c\)](#), the Cu: Mg atomic ratio at the dislocation was also ~ 1 . These figures show that the concentration of Li at the GBs compared with that within the grains are similar, which implies there is no segregation of Li after HPT and subsequent ageing. A limited

amount of Si was also observed with localised enrichment at grain boundaries (Fig. 5(a) and Fig. 6(a)).

T4-HPT and T6-HPT samples show less distinct solute segregation of grain boundary and no solute enriched features related to dislocations, as compared to the post-ageing HPT conditions. Their atom maps are not shown. In all processing conditions, Li shows neither enrichment nor depletion at the grain boundaries.

Co-clustering of Cu and Mg atoms in all materials was evident in the APT maps, shown in Fig. 7(a-f) and identified as clustered/segregated by a separation distance of 0.7 nm and up to containing 50 solute atoms. T4 and T6 materials show a homogenous distribution of Cu-Mg clusters throughout the whole samples. After HPT, solute clusters at GBs were evident in Fig. 7(b and d), which reduce the overall Gibbs free energy and enhance the thermal stability of grain boundaries [44,45]. During final artificial ageing treatment, strong Cu-Mg cluster segregation occurs at both GBs and dislocations (marked with yellow boxes), see atom maps Fig. 7(c and f). A more detailed examination of atom maps reveals that the detected clusters are distributed mainly at the GBs rather than in the matrix, having an average Cu: Mg ratio of ~1 obtained from concentration profiles.



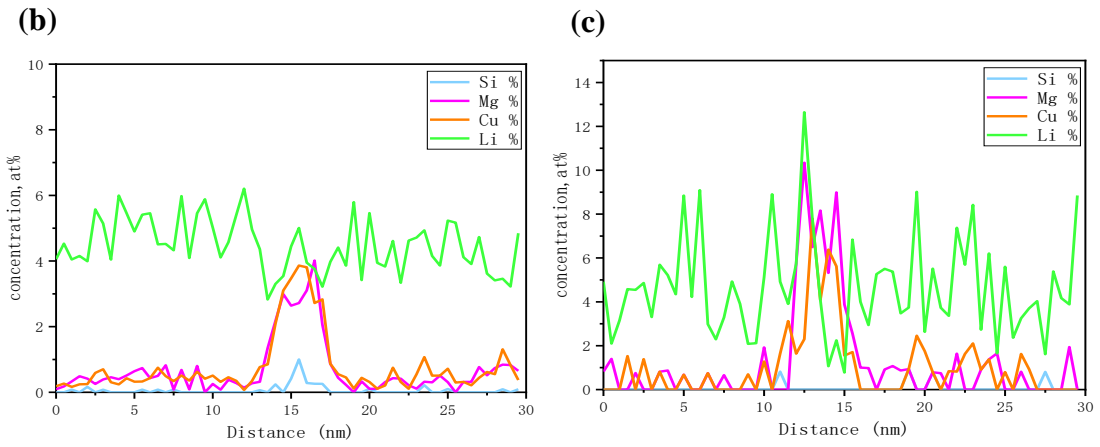


Fig. 5. Atom maps of Al-Cu-Li alloy processed by T4-HPT-AA: (a) Cu, Mg, Li, Si atom maps. (b) concentration profiles of solutes across GB and (c) across dislocation.

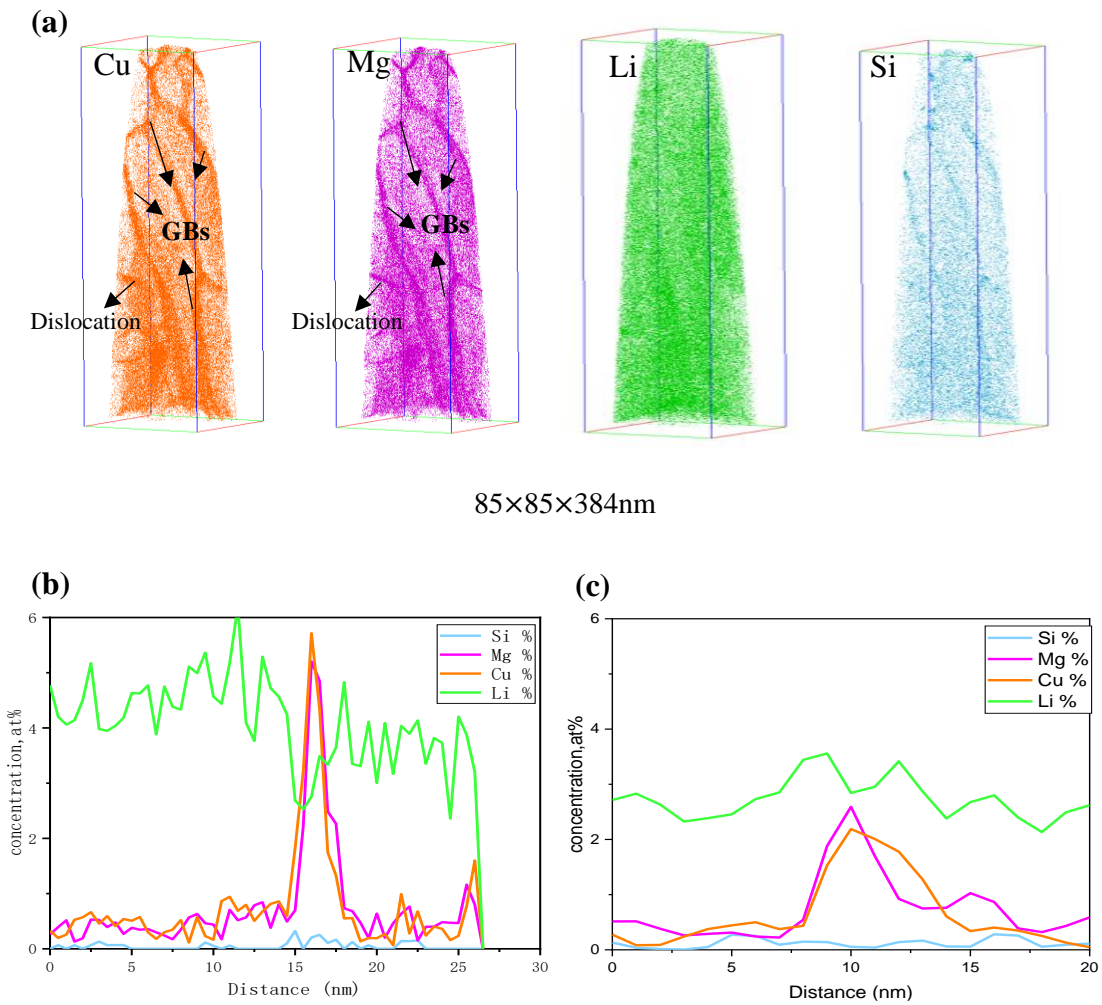


Fig. 6. Atom maps of Al-Cu-Li alloy processed by T6-HPT-AA: (a) Cu, Mg, Li, Si atom maps. (b) concentration profiles of solutes across GB and (c) across dislocation.

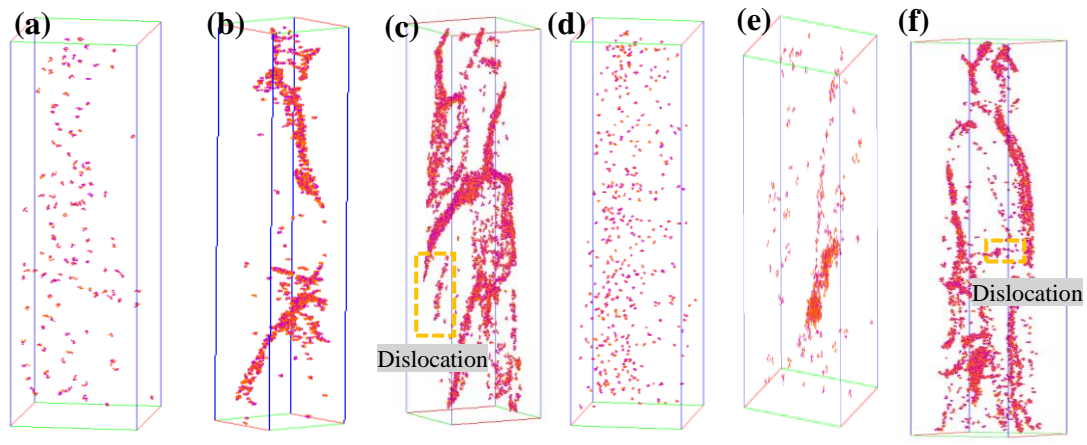


Fig. 7. Distribution of Cu-Mg co-cluster maps in (a) T4, (b) T4-HPT, (c) T4-HPT-AA, (d) T6, (e) T6-HPT, (f) T6-HPT-AA processed Al-Cu-Li alloy.

3.4 DSC data

DSC curves presented in [Fig. 8\(a\)](#) reveal that several thermal reactions occur during heating up to 330 °C. APT maps in [Section 3.3](#) show that the formation of Cu-Mg cluster after natural ageing and artificial ageing occurred, and no other phase was observed. The low temperature sections up to 100 °C in both T4 and T6 samples were found to have no exothermic reactions, which indicates these clusters do not form to 100 °C. On further heating, multiple endothermic effects occur in the T4 material from 100 °C to 270 °C. This implies that the clusters dissolve during DSC heating. The occurrence of 2 endothermic peaks indicates that some of the clusters transform into a more thermodynamically stable metastable phase or cluster before finally dissolving. The T6 sample in the thermogram exhibits thermal effects that are broadly similar ([Fig. 8\(b\)](#)), but the first endothermic reaction shifts to a higher temperature compared to T4 sample. Hence, the T6 ageing treatment has increased the thermal stability of clusters or transformed clusters into more stable structures.

The T4-HPT and T4-HPT-AA samples show no distinct endothermic effect up to 230 °C, indicating that HPT has caused the clusters to transform into a more stable

structure. The APT data indicates that these structures are clusters at grain boundaries and dislocations. The exothermic effect occurring in these HPT processed samples, which reaches its peak at about 240 °C, is attributable to recovery and the formation of precipitate [22,46]. At that stage, the hardness of the material will drastically decrease and therefore has no direct interest in this study.

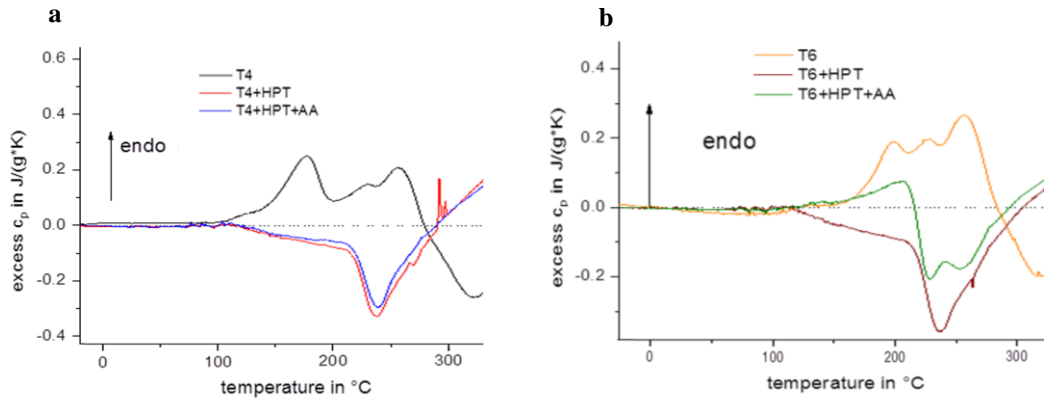


Fig. 8. DSC thermogram of Al-Cu-Li alloy in (a) T4, T4-HPT, T4-HPT-AA and (b) T6, T6-HPT, T6-HPT-AA treatments.

4 Discussion

4.1 Modelling of strength prediction

In order to investigate the dominant mechanisms responsible for the increase in micro-hardness of Al-Cu-Li alloys processed by the combination of HPT and ageing treatments, a model for strengthening is crucial. In this Section, a modified model on the basis of those developed recently [12,47,48] that include multiple strengthening mechanisms will be applied to Al-Cu-Li alloys processed by T4-HPT-AA and T6-HPT-AA conditions. In comparing the model with our experimental data on hardness, an empirical equation $\sigma_y \approx 3HV$ (with units HV and MPa) will be used [49,50].

The yield strength of polycrystalline material is related to the critically resolved shear stress (CRSS) of the grains and the grain boundary strengthening ($\Delta\sigma_{gb}$). In the present

model, we will consider five strengthening mechanisms that affect the CRSS of grains using a linear superposition (see, e.g. [47,48]), which provides:

$$\sigma_y = \Delta\sigma_{gb} + M(\Delta\tau_0 + \Delta\tau_d + \Delta\tau_{ss} + (\Delta\tau_{SRO} + \Delta\tau_m)) \quad (2)$$

Where σ_y is the yield strength; $\Delta\sigma_{gb}$ is strength increase due to grain boundary strengthening; M is often referred to as the Taylor factor [51,52]; the contribution due to dislocation strengthening, $\Delta\tau_d$; the contribution due to solid solution strengthening, $\Delta\tau_{ss}$; and cluster strengthening consists of short-range order strengthening, $\Delta\tau_{SRO}$ [8,9]; and modulus hardening, $\Delta\tau_m$ [53,54]; the intrinsic strength of annealed Al involving small contribution of Mn, Fe, and Si impurities, $\Delta\tau_0$. As XRD, TEM, and APT all reveal no precipitates were formed during HPT and post-ageing, the strengthening due to long-range ordered precipitation will be negligible. The detailed descriptions of each strengthening mechanism are given below.

4.1.1 Strengthening due to grain refinement

The strengthening due to grain boundaries can be defined as follows :

$$\sigma_{gb} = k_{HP}d^{-x} \quad (3)$$

Where k_{HP} is often termed as the Hall-Petch constant [55]; d is the grain size. $x = 1/2$ has been applied in coarse-grained metals for investigating the strengthening behaviours in traditional Hall-Petch relation [56]. $k_{HP} = 0.062 \text{ MPa/m}^{-2}$ was taken here, see Ref [22]. Grain size d was measured from TEM images.

4.1.2 Strengthening due to dislocation strengthening

The strengthening contribution of dislocation is considered to follow the below relation:

$$\sigma_d = M\alpha_1 Gb\sqrt{\rho_{\text{dis}}} \quad (4)$$

Where α_1 is a constant taken as 0.3 [12,22], G is shear modulus (26 GPa for Al), b is burgers vector (0.286 nm for Al) [12,57]; and ρ_{dis} is the dislocation density calculated by microstrain and crystallite size obtained from MAUD software line broadening analysis, see [Eq. \(1\)](#) in Section. 2.

4.1.3 Strengthening due to solid solution

The increment of strength due to solid solution strengthening $\Delta\tau_{\text{ss}}$ is given by:

$$\sigma_{\text{ss}} = M \sum k_j c_j^n \quad (5)$$

Where k_j signifies the strengthening factor for individual elements and c_j indicates the concentrations of the alloying elements in solid solution [58,59], and n is a constant taken as 1 [52,58]. After calculating the solvus of Cu-Mg clusters using thermodynamic data on Al-Cu-Mg alloys [8], and a quantitative evaluation of APT raw data, i.e. the number of Cu and Mg atoms detected within clusters and the total number of Cu and Mg atoms in the sample. We adopt the assumption that 80% of Cu and Mg atoms are clustering in samples and only 20% of them stay in the solid solution, signifying only Li fully contributes to solid solution strengthening. For the present Al-2.88Cu-1.34Li-1.03Mg-0.09Zr wt% alloy, converting into atomic percent provides the composition Al-1.20Cu-5.09Li-1.11Mg-0.03Zr at%. The contribution of Mn, Fe and Si to solution strengthening are very small, much smaller than those of Cu, Li and Mg, and their small contribution will be treated as part of intrinsic strength $\Delta\tau_0$.

4.1.4 New strengthening model due to co-cluster and cluster-defect complexes

The co-cluster strengthening is considered to be due to short-range order strengthening and modulus hardening. The former has been widely studied and proved to be the

dominant cluster strengthening effect in typical Al alloys [8,9,22]. The work done by lattice deformation that is caused by co-clusters impedes the movement of dislocations, and it is equal to the change in energy-related to short-range order per unit area on slip plans in Al matrix. This gives equation [8]:

$$\Delta\tau_{\text{SRO}} = \frac{\gamma_{\text{SRO}}}{b} \quad (6)$$

Where γ_{SRO} is the change in energy per unit area on slip plans on the passing of one dislocation and b is the burgers vector.

Starink and Wang [8] developed a model that provides a detailed calculation regarding the change in area density of A–B nearest neighbour bonds crossing the slip plane on the passing of one dislocation, and thus derived a short-range strengthening equation in which the strengthening is proportional to the enthalpy of formation of the clusters, $\Delta H_{\text{A-B}}$. The APT atom maps in [Fig. 7](#), show that three types of short-range order clusters are present: (i) intragranular solute clusters, i.e. clusters in matrix, (ii) clustering at GBs, (iii) clustering at dislocations. In the present model, we will consider that all three types have a distinct enthalpy of formation associated with them, and hence they will each have a distinct strengthening effect. Our new short-range order clusters strengthening model is then represented as:

$$\Delta\sigma_{\text{SRO-matrix}} \cong M \frac{\Delta H_{\text{A-B}}}{b} \frac{4}{\sqrt{3}b^2} \frac{2}{3} (\gamma_{\text{A,1}} + \gamma_{\text{B,1}}) \quad (7)$$

$$\Delta\sigma_{\text{SRO-gb}} \cong M \frac{\Delta H_{\text{A-B-gb}}}{b} \frac{4}{\sqrt{3}b^2} \frac{2}{3} (\gamma_{\text{A,2}} + \gamma_{\text{B,2}}) \quad (8)$$

$$\Delta\sigma_{\text{SRO-dis}} \cong M \frac{\Delta H_{\text{A-B-dis}}}{b} \frac{4}{\sqrt{3}b^2} \frac{2}{3} (\gamma_{\text{A,3}} + \gamma_{\text{B,3}}) \quad (9)$$

Where $\Delta H_{\text{A-B}}$ stands for the enthalpy of A-B clusters in matrix, $\Delta H_{\text{A-B-gb}}$ is the enthalpy of A-B clusters at the GBs and $\Delta H_{\text{A-B-dis}}$ signifies the enthalpy of A-B clusters at dislocations. $\gamma_{\text{A,1}}$ and $\gamma_{\text{B,1}}$ defined as the number of A atoms and B atoms per volume in the clusters of matrix, respectively; $\gamma_{\text{A,2}}$ and $\gamma_{\text{B,2}}$ are the number of A

atoms and B atoms per volume in the clusters-GBs complexes, respectively; $y_{A,3}$ and $y_{B,3}$ are the number of A atoms and B atoms per volume in the clusters-dislocations complexes, respectively.

As the average Cu/Mg ratio in clusters was close to 1, which has been confirmed by APT data also in accordance with the Cu/Mg ratio estimated by best fitting a thermodynamic model to data on Al-Cu-Mg alloys [8]. Therefore, the following set of equations define the interrelation between the compositions of the two main alloying elements (Cu and Mg):

$$y_{A,1} = y_{B,1} \quad (10)$$

$$y_{A,2} = y_{B,2} \quad (11)$$

$$y_{A,3} = y_{B,3} \quad (12)$$

$$y_{A,total} = y_{B,total} \quad (13)$$

Hence:
$$y_{A,1} + y_{A,2} + y_{A,3} = y_{B,1} + y_{B,2} + y_{B,3} \quad (14)$$

To investigate the amount of A and B atoms (in our alloys Cu and Mg) clustered on the GBs ($y_{A,2}$ and $y_{B,2}$) and dislocations ($y_{A,3}$ and $y_{B,3}$), we consider A and B located around the grain boundary and dislocation as a plane and a cylinder, respectively. Grain boundary density can then be calculated and with the aid of concentration profiles of APT, so that $y_{A,2}$ and $y_{B,2}$ can be obtained. On the other hand, $y_{A,3}$ and $y_{B,3}$ can be calculated utilising dislocation density measured from XRD and solute concentration profiles of APT. Besides, clusters induce an elastic modulus which brings an extra strengthening to Al-Cu-Li alloy [8,9,22,54]. The CRSS caused by shear modulus of clusters can be approximated as:

$$\Delta\sigma_{mod} = M \frac{\Delta\mu}{(4\pi\sqrt{2})} f^{\frac{1}{2}} \quad (15)$$

Where f is the total volume fraction of the clusters, $\Delta\mu$ is the difference in shear modulus between clusters and their surrounding metallic phase. $\Delta\mu = 3.4$ GPa was used for strengthening due to Cu-Mg clusters [22].

4.2 The limitations of the Rietveld method/ misfit of solute atoms

The Rietveld method uses line broadening to determine crystallite size and dislocation density. For analysis, the method assumes that polycrystals contain crystals (grains) separated by grain boundaries with dislocations in the grains. The method analysis of XRD data indicates that artificial ageing (AA) treatment after the T4-HPT and the T6-HPT materials decreases the dislocation density in the materials (see [Fig.3](#)). However, this result is most likely inaccurate because i) APT data shows that the further artificial ageing treatment causes Cu and Mg atoms to cluster at dislocations, which is not considered in the Rietveld analysis method; ii) the hardness of the materials increases after AA treatment whilst APT shows no indication of a known hardening reaction that could compensate for the reduction in dislocation hardening.

It is thought that rather than a reduction in dislocation density, in fact, Cu and Mg clustering at dislocations during the final ageing stage reduces the local nanostrains. In the Al-rich phase, the atomic radius of Mg is larger than Al whilst Cu is smaller than Al. Cu and Mg atoms segregate around dislocation will find atomic sites more suited to their radii. Cu and Mg atoms will preferentially move to these positions because it reduces the free energy of the sample (e.g. this positioning reduces local strain fields). Thus, they can effectively reduce nanostrains, causing a narrowing of the diffraction peaks. The Rietveld analyses such a narrowing diffraction peak, finds a lower microstrain and ascribes it to a lower density of defects (e.g. dislocations). Hence, the dislocation density then should be unaltered.

We can now assume that the dislocation density after HPT remains unaltered during subsequent low temperature ageing in the strength model. In support of the above interpretation, it is noted that in published works on post SPD ageing of Al and its alloys, generally no reduction in dislocation density was reported for the low artificial ageing temperature applied in this work [12,15]. Instead, reduction in dislocation density was reported in AA6069 during ECAP processing at 170 °C [60] and in AA7036 during ECAP processing at 200 °C due to annihilation of dislocations [61].

4.3 Estimating enthalpy of Cu-Mg clusters at dislocations

ΔH_{A-B} was identified as 34.5 ± 0.5 kJ/mol using calorimetry data on coarse grained Al-Cu-Mg alloys [8] and ΔH_{A-B-gb} was determined as 50 ± 5 kJ/mol using data on UFG Al-Cu-Mg alloys [62]. Ageing of the HPT processed materials does not alter the clustering at the GBs to any detectable extent, and instead the formation of clusters at dislocations is the main change that is observed. This indicates that the formation of dislocation-cluster complexes causes the largest decrease in free energy, i.e. it suggests that $\Delta H_{A-B-dis} > \Delta H_{A-B-gb} > \Delta H_{A-B}$. In the analysis of $\Delta H_{A-B-dis}$ we could attempt to consider from dislocation elastic energy aspect. Dislocations in a crystal increase the elastic energy of the material predominantly due to elastic lattice distortion. However, clustering of Cu and Mg atoms around a dislocation can be very effective in reducing the elastic energy due to size effects of Mg and Cu atoms. The expression for elastic energy caused by lattice distortion is [63]:

$$U_{el} = \frac{Gb^2}{4\pi(1-\nu)} \ln \frac{R}{r} (1 - \nu \cos^2 \alpha) \quad (16)$$

Where U_{el} is the elastic energy associated with a dislocation, G is shear modulus, 26 GPa was taken to use here, b is burgers vector, ν is Poisson's ratio, 0.3 was used for Al alloy, r_o is the core radius of the dislocation ($r_o = 2b$), α is a geometrical factor that

represents the angle between the burgers vector and the dislocation line. For screw dislocation, $\alpha = 0$; for edge dislocation, $\alpha = \pi/2$, R is the outer radius of dislocation or dislocation spacing can be determined by:

$$R = \rho_{dis}^{-\frac{1}{2}} \quad (17)$$

Where ρ_{dis} is dislocation density, $R = 100$ nm (valid for a dislocation density 1×10^{14} m⁻², which is typical for HPT processed Al-Cu-Mg type alloys).

The free energy change of the dislocations-containing lattice due to clustering of Cu and Mg atoms around dislocations can be calculated by assuming that the change in elastic energy is the dominant factor the clustering can effectively dissipate all of the elastic energy due to the dislocation. The total enthalpy changes due to clustering near the dislocation will be the sum of the change due to the elastic strain field plus the change due to near neighbour Cu-Mg interactions. From the above we may thus conclude that a good approximation for $\Delta H_{A-B-dis} \approx 165$ kJ/mol.

4. 4 The combination of multiple strengthening mechanisms

The values of the parameters involved in the strength prediction model are all derived from either the experimental results presented in [Section 3](#) or literature data. A list of parameters is shown in [Table 2](#). The relation between Vickers hardness and yield strength is approximate $HV = \frac{\sigma_y}{C}$, where C is a constant that is often taken as ~ 3 , see Refs [49,64]. In our strengthening model, the equation of $\sigma_y \approx 3HV$ is taken for assessment, where the unit of HV has converted into MPa for easy comparison. The results of the model predictions are illustrated in [Fig. 9](#). The corresponding values of each strengthening mechanism are listed in [Table 3](#). The yield strength of six processing

condition groups is given, and each group represents the comparison of the yield strength predicted by strengthening model and the strength measured from hardness results. The graph shows a good correspondence between the strength predicted by the model and the measured strength from Vickers hardness for T4, T4-HPT, T4-HPT-AA, T6, T6-HPT processed samples. Among the model predictions for total strength, only the prediction of strength of T6-HPT-AA sample is substantially outside the typical accuracy of 4%, and it is most likely due to the estimation of $\Delta H_{A-B-dis}$ value. This analysis shows that grain boundary strengthening is still the crucial mechanism for HPT-processed materials, but it accounts for only ¼ of the total strength. The Cu-Mg clusters contribute substantially to the strength in all conditions. The combined effect of all three types of clusters due to short-range order mechanism is dominant for all conditions studied, with less than 8% of the modulus strengthening effect. Therefore, the whole clusters in total have the strengthening larger than grain boundaries.

Table 2. Parameters used in the strengthening prediction model.

Parameters	Values	Refs
M	2.6	[51,52]
k_{HP}	0.062 MPa/m ²	[65]
$\Delta\tau_0$	10 MPa	[51,52]
α_1	0.3	[50]
G	26 GPa	[50]
K_{Cu}	10 MPa/at% Cu	[52,58]
K_{Mg}	6 MPa/at% Mg	[58,66]
K_{Li}	6 MPa/at% Li	[67]
n	1	[66]
c_{Cu}	1.20 at%	See Section 4.1.3
c_{Mg}	1.11 at%	See Section 4.1.3
c_{Li}	5.09 at%	See Section 4.1.3
b	0.286 nm	[51,52]
ΔH_{A-B}	34.5 kJ/mol	[8]
ΔH_{A-B-GB}	50 kJ/mol	[12]
$\Delta H_{A-B-dis}$	135 kJ/mol	See Section 4.3
C	3	[49]
$\Delta\mu$	3.4 GPa	[22]

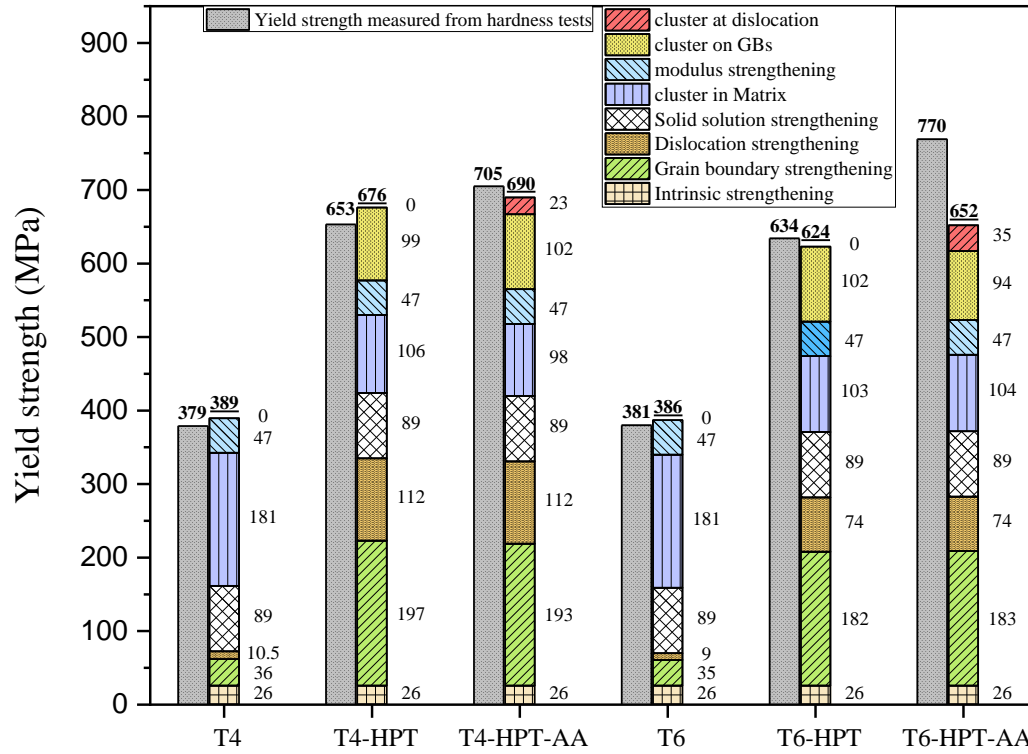


Fig. 9. Comparison between yield strength measured from strengthening model and micro-hardness tests.

Table 3

Measured strength (MPa) by Vickers harness and strength (MPa) caused by different strengthening mechanisms in six processing conditions.

Conditions	Hv	σ_0	σ_{gb}	$\sigma_{\rho_{dis}}$	σ_{ss}	$\sigma_{SRO-matrix}$	σ_{mod}	σ_{SRO-gb}	$\sigma_{SRO-dis}$
T4	379	26	36	10.5	89	181	47	0	0
T4-HPT	653	26	197	112	89	106	47	99	0
T4-HPT-AA	705	26	193	112	89	98	47	102	23
T6	381	26	35	9	89	181	47	0	0
T6-HPT	634	26	182	74	89	103	47	102	0
T6-HPT-AA	770	26	183	74	89	104	47	94	35

5 Conclusion

This present experimental work demonstrates the potential for combining grain refinement with appropriate ageing treatments to achieve an ultra-high strength for Al-Cu-Li alloy. Two processing conditions were applied to two types of materials: T4-HPT-AA and T6-HPT-AA. A series of characterisation techniques, e.g. XRD, TEM,

APT and DSC were conducted on the materials with different processing conditions. A strengthening model was used to evaluate the contributions of different strengthening effects. The following conclusions are reached:

1. T4-HPT-AA treatment of the Al-Li-Cu alloy has accomplished a hardness of ~240 Hv. A further increase in hardness up to ~260 Hv was achieved through pre-HPT ageing at 110 °C/24h and post-HPT ageing at 110 °C/180h, i.e. T6-HPT-AA. This gives rise to more than twice the hardness of the sample that had undergone T4 heat treatment.
2. The grain size of T4 and T6-processed samples were significantly refined (by a factor of ~10) during HPT deformation, resulting in an UFG structure with grain size of ~80 nm and ~115 nm, respectively. This UFG structure was retained during subsequent artificial ageing at 110 °C/60h in T4-HPT-AA and 110 °C/180h in T6-HPT-AA conditions.
3. Homogeneously distributed Cu-Mg clusters were observed throughout the T4 and T6 samples. During HPT process, the Cu-Mg clusters segregate strongly at the UFG grain boundaries of T4 and T6 materials, and segregation of solute co-cluster at dislocations was revealed during final artificial ageing at 110 °C.
4. The assessment of strengthening mechanisms has shown that all three types of short-range order strengthening due to clustering contribute to the high strength of HPT-processed Al-Cu-Li alloy.
5. 5 out of 6 predictions show a good correspondence between measured and predicted values.

Data availability

All data included in this study are available upon request by contact with the corresponding author.

CRedit authorship contribution statement

Jiahui Dong: Conceptualisation, Methodology, Data curation, Project administration, Writing – original draft, Writing – review & editing. Nong Gao: Conceptualisation, Supervision, Writing – review & editing. Marco J Starink: Conceptualisation, Supervision, Writing – review & editing. Ying Chen: Methodology, Writing - review & editing. Lingfei Cao and Hui Song: Methodology, Writing – review & editing. Hannes Fröck and Benjamin Milkereit: Methodology, Writing – review & editing.

Declaration of competing interest

The authors declare that they have no known competing financial interests or personal relationships that could have appeared to influence the work reported in this paper.

Acknowledgements

This work was financially supported by the Faculty of Engineering and the Environment at the University of Southampton. In addition, we gratefully acknowledge the experimental support of TEM from the Xiamen University of Technology, China, APT provided by the Electron Microscopy Centre of Chongqing University and financially supported by the National Natural Science Foundation of China (51871033). Also appreciate the University of Rostock, Germany, for assistance in DSC experiments.

References

- [1] N. Prasad, A. Gokhale, R. Wanhill, Aluminum-lithium alloys: processing, properties, and applications, 2013.
- [2] T Warner, Recently-developed aluminium solutions for aerospace applications, *Mater. Sci. Forum.* 519–521 (2006) 1271–1278.
- [3] N. Nayan, N.P. Gurao, S.N. Murty, A.K. Jha, B. Pant, S.C. Sharma, K.M. George., Microstructure and micro-texture evolution during large strain deformation of an aluminium–copper–lithium alloy AA 2195, *Mater. Des.* 65 (2015) 862–868.
- [4] T. Dursun, C. Soutis, Recent developments in advanced aircraft aluminium alloys, *Mater. Des.* 56 (2014) 862–871.
- [5] J.R. Davis, ASM specialty handbook, Alum. Alum. Alloy. (1993) 207–216.
- [6] C.F. Tan, S.M. Radzai, Effect of hardness test on precipitation hardening aluminium alloy 6061-T6, *Chiang Mai J. Sci.* 36 (2009) 276–286.
- [7] A.P. Zhilyaev, T.G. Langdon, Using high-pressure torsion for metal processing: Fundamentals and applications, *Prog. Mater. Sci.* 53 (2008) 893–979.
- [8] M. Starink, S. Wang, The thermodynamics of and strengthening due to co-clusters: general theory and application to the case of Al–Cu–Mg alloys, *Acta Mater.* 57 (2009) 2376–2389.
- [9] M. Starink, L. Cao, P. A. Rometsch, A model for the thermodynamics of and strengthening due to co-clusters in Al–Mg–Si-based alloys, *Acta Mater.* 60 (2012) 4194–4207.
- [10] L.T. Stephenson, M.P. Moody, P. V Liddicoat, S.P. Ringer, New techniques for the analysis of fine-scaled clustering phenomena within atom probe tomography (APT) data, *Microsc. Microanal.* 13 (2007) 448.
- [11] M.J. Starink, N. Gao, J.L. Yan, The origins of room temperature hardening of Al–Cu–Mg alloys, *Mater. Sci. Eng.* 387–389 (2004) 222–226.
- [12] Y. Chen, N. Gao, G. Sha, S. Ringer, M. Starink, Strengthening of an Al–Cu–Mg alloy processed by high-pressure torsion due to clusters, defects and defect–cluster complexes, *Mater. Sci. Eng.* 627 (2015) 10–20.
- [13] W. Sun, X. Qiao, M. Zheng, X. Zhao, H. Chen, Achieving ultra-high hardness

- of nanostructured Mg-8.2 Gd-3.2 Y-1.0 Zn-0.4 Zr alloy produced by a combination of high pressure torsion and ageing treatment, *Scr. Mater.* 155 (2018) 21–25.
- [14] P. Liddicoat, X. Liao, Y. Zhao, Y. Zhu, Nanostructural hierarchy increases the strength of aluminium alloys, *Nature*. 1 (2010) 1–7.
- [15] G. Sha, K. Tugcu, X.Z. Liao, P.W. Trimby, My. Murashkin, R.Z. Valiev, S.P. Ringer, Strength, grain refinement and solute nanostructures of an Al–Mg–Si alloy (AA6060) processed by high-pressure torsion, *Acta Mater.* 63 (2014) 169–179.
- [16] M.F. Ashby, The deformation of plastically non-homogeneous materials, *Philos. Mag.* 21 (1970) 399–424.
- [17] K. Marthinsen, E. Nes, A general model for metal plasticity, *Mater. Sci. Eng.* 234–236 (1997) 1095–1098.
- [18] Y. Estrin, L. Toth, A. Molinari, Y. Bréchet, A dislocation-based model for all hardening stages in large strain deformation, *Acta Mater.* 46 (1998) 5509–5522.
- [19] O. Rezvanian, M. Zikry, Inelastic contact behavior of crystalline asperities in rf MEMS devices, *Eng. Mater. Technol.* 131 (2009) 011002-1-011002–10.
- [20] G. Nurislamova, X. Sauvage, M. Murashkin, R. Islamgaliev, R. Valiev, Nanostructure and related mechanical properties of an Al–Mg–Si alloy processed by severe plastic deformation, *Philos. Mag. Lett.* 88 (2008) 459–466.
- [21] G. Sha, L. Yao, X. Liao, S. Ringer, Z. Duan, Segregation of solute elements at grain boundaries in an ultrafine grained Al–Zn–Mg–Cu alloy, *Ultramicroscopy*. 111 (2011) 500–505.
- [22] Y. Chen, N. Gao, G. Sha, S. Ringer, M.S.-A. Materialia, undefined 2016, Microstructural evolution, strengthening and thermal stability of an ultrafine-grained Al–Cu–Mg alloy, Elsevier. (n.d.).
- [23] A.P. Zhilyaev, T.R. McNelley, T.G. Langdon, Evolution of microstructure and microtexture in fcc metals during high-pressure torsion, *J. Mater. Sci.* 42 (2007) 1517–1528.
- [24] C. Xu, M. Furukawa, Z. Horita, T.G. Langdon, The evolution of homogeneity and grain refinement during equal-channel angular pressing: A model for grain refinement in ECAP, *Mater. Sci. Eng. A.* 398 (2005) 66–76.
- [25] A. Vorhauer, R. Pippan, On the homogeneity of deformation by high pressure

- torsion, *Scr. Mater.* 51 (2004) 921–925.
- [26] M.H. Shaeri, M.T. Salehi, S.H. Seyyedein, M.R. Abutalebi, J.K. Park, Microstructure and mechanical properties of Al-7075 alloy processed by equal channel angular pressing combined with aging treatment, *Mater. Des.* 57 (2014) 250–257.
- [27] M. Vaseghi, A.K. Taheri, S.I. Hong, H.S. Kim, Dynamic ageing and the mechanical response of Al–Mg–Si alloy through equal channel angular pressing, *Mater. Des.* 31 (2010) 4076–4082.
- [28] K. Ohashi, T. Fujita, K. Kaneko, Z. Horita, T.G. Langdon, The aging characteristics of an Al–Ag alloy processed by equal-channel angular pressing, *Mater. Sci. Eng. A.* 437 (2006) 240–247.
- [29] J.K. Kim, H.G. Jeong, S.I. Hong, Y.S. Kim, W.J. Kim, Effect of aging treatment on heavily deformed microstructure of a 6061 aluminum alloy after equal channel angular pressing, *Scr. Mater.* 45 (2001) 901–907.
- [30] Z. Horita, K. Ohashi, T. Fujita, K. Kaneko, T.G. Langdon, Achieving high strength and high ductility in precipitation-hardened alloys, *Adv. Mater.* 17 (2005) 1599–1602.
- [31] N. Kamp, M.J. Starink, I. Sinclair, N. Gao, P.J. Gregson, P.D. Pitcher, S. Gardiner, Development of Al-Cu-Mg-Li (Mn,Zr,Sc) alloys for age-forming, *Mater. Forum.* 28 (2004) 369–375.
- [32] L. Lutterotti, S. Gialanella, X-ray diffraction characterisation of heavily deformed metallic specimens, *Acta Mater.* 46 (1998) 101–110.
- [33] L.B. McCusker, R.B. Von Dreele, D.E. Cox, D. Louër, P. Scardi, Rietveld refinement guidelines, *J. Appl. Crystallogr.* 32 (1999) 36–50.
- [34] Y.H. Zhao, X.Z. Liao, Z. Jin, R.Z. Valiev, Y.T. Zhu, Microstructures and mechanical properties of ultrafine grained 7075 Al alloy processed by ECAP and their evolutions during annealing, *Acta Mater.* 52 (2004) 4589–4599.
- [35] R.K.W. Marceau, G. Sha, R.N. Lumley, S.P. Ringer, Evolution of solute clustering in Al–Cu–Mg alloys during secondary ageing, *Acta Mater.* 58 (2010) 1795–1805.
- [36] G. Madhu, V.C. Bose, K. Maniammal, A.S.A. Raj, V. Biju, Microstrain in nanostructured nickel oxide studied using isotropic and anisotropic models, *Phys. B Condens. Matter.* 421 (2013) 87–91.
- [37] K. Maniammal, G. Madhu, V. Biju, X-ray diffraction line profile analysis of

- nanostructured nickel oxide: shape factor and convolution of crystallite size and microstrain contributions, *Phys. E Low-Dimensional Syst. Nanostructures*. 85 (2017) 214–222.
- [38] M.J. Starink, X.G. Qiao, J. Zhang, N. Gao, Predicting grain refinement by cold severe plastic deformation in alloys using volume averaged dislocation generation, *Acta Mater.* 57 (2009) 5796–5811.
- [39] N. Ryum, Precipitation and recrystallisation in an Al-0.5 WT.% Zr-alloy, *Acta Metall.* 17 (1969) 269–278.
- [40] F.W. Gayle, J.B. Vander Sande, “Composite” precipitates in an Al-Li-Zr alloy, *Scr. Metall.* 18 (1984) 473–478.
- [41] P.J. Gregson, H.M. Flower, δ' precipitation in Al-Li-Mg-Cu-Zr alloys, *J. Mater. Sci. Lett.* 3 (1984) 829–834.
- [42] J.M. Galbraith, M.H. Tosten, P.R. Howell, On the nucleation of θ' and T 1 on Al 3 Zr precipitates in Al-Li-Cu-Zr alloys, *J. Mater. Sci.* 22 (1987) 27–36.
- [43] S. Lee, Z. Horita, S. Hirosawa, K. Matsuda, Age-hardening of an Al–Li–Cu–Mg alloy (2091) processed by high-pressure torsion, *Mater. Sci. Eng. A*. 546 (2012) 82–89.
- [44] X. Sauvage, N. Enikeev, R. Valiev, Y. Nasedkina, M. Murashkin, Atomic-scale analysis of the segregation and precipitation mechanisms in a severely deformed Al–Mg alloy, *Acta Mater.* 72 (2014) 125–136.
- [45] T. Chookajorn, H.A. Murdoch, C.A. Schuh, Design of stable nanocrystalline alloys, *Science* (80-.). 337 (2012) 951–954.
- [46] S.K. Moghanaki, M. Kazeminezhad, Effects of non-isothermal annealing on microstructure and mechanical properties of severely deformed 2024 aluminum alloy, *Trans. Nonferrous Met. Soc. China*. 27 (2017) 1–9.
- [47] X.G. Qiao, N. Gao, M.J. Starink, A model of grain refinement and strengthening of Al alloys due to cold severe plastic deformation, *Philos. Mag.* 92 (2012) 446–470.
- [48] J. Zhang, N. Gao, M.J. Starink, Microstructure development and hardening during high pressure torsion of commercially pure aluminium: Strain reversal experiments and a dislocation based model, *Mater. Sci. Eng. A*. 528 (2011) 2581–2591.
- [49] P. Zhang, S.X. Li, Z.F. Zhang, General relationship between strength and hardness, *Mater. Sci. Eng. A*. 529 (2011) 62–73.

- [50] C. Qiao, Z. Chen, Y. Zeng, L. Xu, Optimal Strategy-Proof Wireless Resources Auction, in: 2011 Int. Conf. Netw. Comput. Inf. Secur., IEEE, 2011: pp. 446–450.
- [51] M.J. Starink, S.C. Wang, A model for the yield strength of overaged Al–Zn–Mg–Cu alloys, *Acta Mater.* 51 (2003) 5131–5150.
- [52] S.C. Wang, Z. Zhu, M.J. Starink, Estimation of dislocation densities in cold rolled Al–Mg–Cu–Mn alloys by combination of yield strength data, EBSD and strength models, *J. Microsc.* 217 (2005) 174–178.
- [53] E. Nembach, Precipitation hardening caused by a difference in shear modulus between particle and matrix, *Phys. Status Solidi.* 78 (1983) 571–581.
- [54] P. Gomiero, Y. Brechet, F. Louchet, A. Tourabi, B. Wack, Microstructure and mechanical properties of a 2091 AlLi alloy—II. Mechanical properties: Yield stress and work hardening, *Acta Metall. Mater.* 40 (1992) 857–861.
- [55] S.N. Naik, S.M. Walley, The Hall–Petch and inverse Hall–Petch relations and the hardness of nanocrystalline metals, *J. Mater. Sci.* 55 (2020) 2661–2681.
- [56] E.O. Hall, The deformation and ageing of mild steel III discussion of results, *Proc. Phys. Soc. Sect. B.* 64 (1951) 747.
<https://doi.org/https://doi.org/10.1088/0370-1301/64/9/303>.
- [57] I.F. Mohamed, Y. Yonenaga, S. Lee, K. Edalati, Z. Horita, Age hardening and thermal stability of Al–Cu alloy processed by high-pressure torsion, *Mater. Sci. Eng. A.* 627 (2015) 111–118.
- [58] M.J. Starink*, N. Gao, L. Davin, J. Yan, A. Cerezo, Room temperature precipitation in quenched Al–Cu–Mg alloys: a model for the reaction kinetics and yield strength development, *Philos. Mag.* 85 (2005) 1395–1417.
- [59] H.R. Shercliff, M.F. Ashby, A process model for age hardening of aluminium alloys—I. The model, *Acta Metall. Mater.* 38 (1990) 1789–1802.
- [60] M. Cai, D.P. Field, G.W. Lorimer, A systematic comparison of static and dynamic ageing of two Al–Mg–Si alloys, *Mater. Sci. Eng. A.* 373 (2004) 65–71.
- [61] G. Sha, Y.B. Wang, X.Z. Liao, Z.C. Duan, S.P. Ringer, T.G. Langdon, Influence of equal-channel angular pressing on precipitation in an Al–Zn–Mg–Cu alloy, *Acta Mater.* 57 (2009) 3123–3132.
- [62] Y. Chen, N. Gao, G. Sha, S. Ringer, MJ Starink, Microstructural evolution, strengthening and thermal stability of an ultrafine-grained Al–Cu–Mg alloy,

- Acta Mater. 109 (2016) 202–212.
- [63] D. Hull, D.J. Bacon, Chapter 4 - Elastic Properties of Dislocations, in: *Introductory to Dislocations*, 5th ed., Butterworth-Heinemann, Oxford, 2011: pp. 63–83.
<https://doi.org/https://doi.org/10.1016/B978-0-08-096672-4.00004-9>.
- [64] J.W. Zhang, M.J. Starink, N. Gao, W.L. Zhou, Influence of Strain Reversals during High Pressure Torsion Process on Strengthening in Al-Cu-Mg (-Li) Alloy, in: *Mater. Sci. Forum*, Trans Tech Publ, 2011: pp. 809–814.
- [65] M.J. Starink, X. Cheng, S. Yang, Hardening of pure metals by high-pressure torsion: a physically based model employing volume-averaged defect evolutions, *Acta Mater.* 61 (2013) 183–192.
- [66] Ø. Ryen, B. Holmedal, O. Nijs, E. Nes, E. Sjölander, H.-E. Ekström, Strengthening mechanisms in solid solution aluminum alloys, *Metall. Mater. Trans. A.* 37 (2006) 1999–2006.
- [67] M.J. Starink, P.J. Gregson, Hardness profiles of solution treated SiC p-reinforced Al-Li-Cu-Mg-Zr sheet, *J. Mater. Sci. Lett.* 14 (1995) 1767–1769.